I&EC research
Industrial & Engineering Chemistry Research
pubs.acs.org/IECR
Article

Magnetic-Field Assisted Gas Desorption from Fe_2O_3/Zeolite 13X Sorbent Monoliths for Biogas Upgrading

Kyle Newport, Khaled Baamran, Ali A. Rownaghi, and Fateme Rezaei*

Cite This: *Ind. Eng. Chem. Res.* 2022, 61, 18843−18853
Read Online

ABSTRACT: Magnetic induction has emerged as an attractive method for regenerating adsorbents during separation processes. In this work, we investigated the applicability of magnetic composite sorbents comprising Fe_2O_3 and zeolite 13X in biogas upgrading via a magnetic induction process. The sorbent materials with 10, 15, and 20 wt % Fe_2O_3 content were formulated into monolithic contactors via additive manufacturing and their physiochemical and magnetic properties were assessed accordingly. The effects of Fe_2O_3 particle size, magnetic field intensity, and monolith composition and configuration on CO_2 and CH_4 desorption rates as well as heating and cooling rates were systematically investigated. Our results indicated that 5 μm-size Fe_2O_3 with a loading of 20 wt % in the composite is the best performing material exhibiting heating, cooling, and desorption rates of 6.56 °C/min, 3.84 °C/min, and 0.25 mmol CO_2/g min, respectively. It was also found that the layer-by-layer printing approach outperforms the homogenously mixed method in formulating magnetic monoliths by exhibiting heating, cooling, and desorption rates of 7.78 °C/min, 4.89 °C/min, and 0.376 mmol CO_2/g min, respectively. Lastly, the advantage of induction heating over traditional heating in quickly regenerating the adsorbent was demonstrated. This work highlights the suitability of the induction heating method in upgrading biogas as a renewable source of energy.

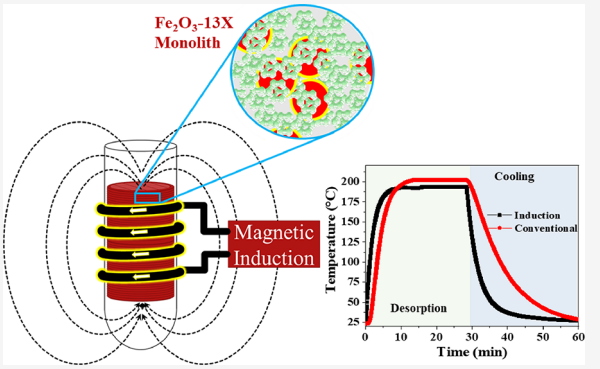

1. INTRODUCTION

Achieving net-zero emissions by the mid-century while utilizing sustainable bioresources has become a priority for energy leaders globally.[1] In that regard, utilizing abundant, stranded biogas produced from municipal and agricultural biowastes not only provides a renewable source of energy but also offers a sustainable platform toward a green and net-zero economy in that the upgraded methane can be injected directly into the natural gas pipelines while the separated carbon dioxide can be used in the production of other value-added products or stored.[2−4] On the other hand, electrifying separation processes are necessary to reduce their thermal-energy dependency and achieve a net-zero economy by 2050, mainly because such separations are extremely energy-intensive, consuming roughly about 10−15% of the total energy worldwide.[5]

With the energy crisis in Europe, other sources of fuel are becoming more prevalent due to Europe's dependence on foreign fuel sources.[6] Biogas can be produced from micro-organisms that feed on biowaste through a process called anaerobic digestion, leading to the final step of methanation. The product of this process leads to a gas composition of CO_2 and CH_4 in ratios of ∼50:50 vol % but also can contain trace amounts of hydrogen sulfide (H_2S) or ammonia (NH_3).[7] For applications such as pipeline-grade fuel, the CH_4 purity must be above 95%.[7] To achieve this goal, upgrading the biogas, which is essentially a separation process where CO_2 and other impurities are removed from CH_4, is required. The main technologies considered for biogas upgrading include absorption via amine scrubbing and pressurized water scrubbing, adsorption via pressure swing adsorption (PSA), and membrane via gas permeation.[8−10]

Adsorption-based separation has the potential to adopt non-thermal practices for regeneration of sorbents such as electric swing adsorption (ESA),[9] magnetic induction swing adsorption (MISA),[11,12] or microwave swing adsorption (MSA).[13] In particular, magnetic responsiveness is a valuable characteristic that can be exploited to address the problem of high-energy requirements of separation processes, as magnetic field-induced heating can be used for desorption, with the heat generated homogeneously through the material due to localized nanoheaters, and thus is preferred for the adsorbents

Received: August 23, 2022
Revised: November 20, 2022
Accepted: December 2, 2022
Published: December 19, 2022

https://doi.org/10.1021/acs.iecr.2c02969
Ind. Eng. Chem. Res. 2022, 61, 18843−18853

with low thermal conductivity where the heating time can be greatly reduced. This method offers substantial advantages over conventional heating methods including (i) greatly reducing heating time due to the generation of local heat from inside to outside, (ii) avoiding additional heat losses involved in traditional heating methods, (iii) overcoming the intrinsic heat conductivity shortcoming of most sorbent materials, and (iv) avoiding classical trade-offs such as correlation of selectivity and heat of regeneration in smart magnetic sorbents.

In an external magnetic field, magnetic nanoparticles integrated into sorbents convert the magnetic field to thermal energy by acting as nanoheaters, hence allowing for fast and complete regeneration (under optimized conditions). Magnetic field-responsive sorbents generate local heat due to the static hysteresis and dynamic core losses of magnetic nanoparticles. Although the development of stimulus-responsive sorbents is a promising research field for adsorptive separation, the current studies are still in their infancy stage.[11,14,15] A few previous works demonstrated the quick release of adsorbed CO_2 through rapid internal temperature increase in magnetic sorbents consisting of $MgFe_2O_4$ particles, incorporated in metal−organic frameworks (MOFs), such as UiO-66 and Mg-MOF-74.[16−19] Gholami et al.[11] reported one order of magnitude faster desorption rate at high coil currents for extrudates of composite sorbents containing 13X zeolite and Fe_3O_4 than under conventional heating. Most recently, we developed novel composites of Fe_2O_3@MOF-74 composites and investigated their adsorption performance in ethane/ethylene separation.[12] The reported results demonstrated the suitability of these types of magnetic-responsive sorbents for olefin/paraffin separations.

Although zeolite 13X is a benchmark sorbent for CO_2 capture with high working capacity and selectivity in most cases, it is not ferromagnetic, which makes it unsuitable for MISA applications.[20−22] A viable solution to address this drawback is to mix it with ferromagnetic particles such as Fe_2O_3 or Fe_3O_4 that can act as nanoheaters upon exposure to an external magnetic field to enhance the overall heat flow, thereby generating local heat and regenerating the sorbent.[10,11] On the other hand, assessing the effectiveness of the sorbent materials at the lab scale in the form factors suitable for industrial applications is required to bridge the gap between the laboratory research and large-scale implementation. Although extrusion is the current method of fabricating monolithic structures, recent studies have shown that additive manufacturing offers an alternative formulation method, which enables fabrication of complex geometries with desired configurations and unique mechanical and structural properties.[34]

In this work, we aimed at maximizing the effectiveness of 3D-printed monoliths of Fe_2O_3/zeolite 13X composites in biogas upgrading by optimizing the magnetic particles' size and composition as well as the configuration of printed monoliths. Moreover, the effect of magnetic field intensity on desorption was investigated and the results were compared with those of thermal heating to highlight the advantage of induction heating over the conventional heating method.

2. EXPERIMENTAL SECTION

2.1. Materials. The commercial zeolite 13X with a particle size of ∼2 μm was purchased from Sigma Aldrich. The ferromagnetic particles used to achieve the induction heating were Fe_2O_3 particles of 5 μm size and obtained from Sigma Aldrich, while the 30 and 100 nm particle sizes were purchased from US Research Nanomaterials Inc. The binder used in the monoliths was nanoporous bentonite clay from Sigma Aldrich. The gasses used in the adsorption tests (argon and 50:50 vol % CO_2/CH_4 mixture) were all of UHP grade and purchased from Airgas.

2.2. Magnetic Monoliths Printing. The monolith pastes were prepared using 10 wt % bentonite clay, 4 wt % methylcellulose, and 10, 15, and 20 wt % Fe_2O_3, with the remaining amount filled with the zeolite 13X sorbent. Water was used as the solvent and added to saturate the powder and mixed using a ball mill roller mixer method. The paste was then dried till the paste could hold its shape and then printed in a 200 cells per square inch (cpsi) honeycomb structure using the homogenously mixed and layer-by-layer (LBL) methods, as shown in Figure 1. In the former method, Fe_2O_3 and zeolite 13X were premixed in the paste, whereas in the LBL method, pure pastes of zeolite 13X and Fe_2O_3 were printed in alternate layers. After printing, the monoliths were dried overnight and then calcined at 550 °C using a ramp rate of 10 °C/min for 6 h. This calcination step was carried out to burn out the methylcellulose plasticizer, aiming at creating mesoporous pathways within the monolith.

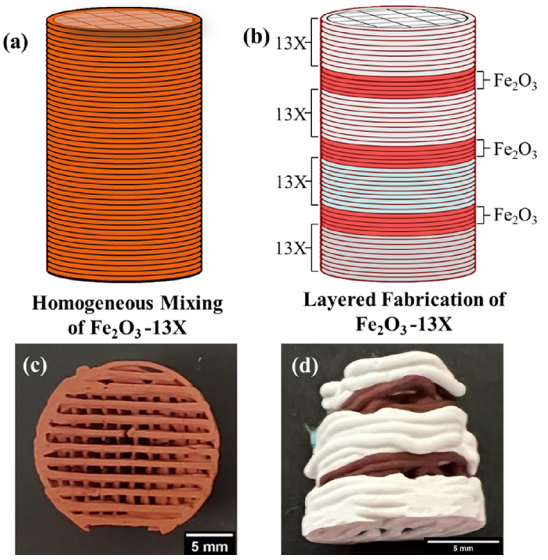

Figure 1. Printing strategy schematics of (a, b) the designed monoliths and (c, d) their corresponding 3D-printed counterparts.

2.3. Materials Characterization. The textural properties of the samples were analyzed by N_2 physisorption measurements at 77 K on a Micromeritics 3Flex gas analyzer. The samples were degassed at 350 °C for 6 h at a ramp rate of 10 °C/min. The surface area and pore size distribution (PSD) of the materials were calculated using physisorption data from the Brunauer−Emmet−Teller (BET) and the non-local density functional theory (NLDFT) methods, respectively. The NLDFT method used an ideal pore-slit model for the calculation of theoretical N_2 isotherms. The electron paramagnetic resonance (EPR) test was conducted on a Bruker benchtop ESR 5000 instrument. All the samples were exposed to a magnetic field in the range of 50−550 mT, and the EPR intensity was recorded. The specific heat absorption (SAR) measurement was was carried out by dispersing Fe_2O_3-13X

https://doi.org/10.1021/acs.iecr.2c02969
Ind. Eng. Chem. Res. 2022, 61, 18843−18853

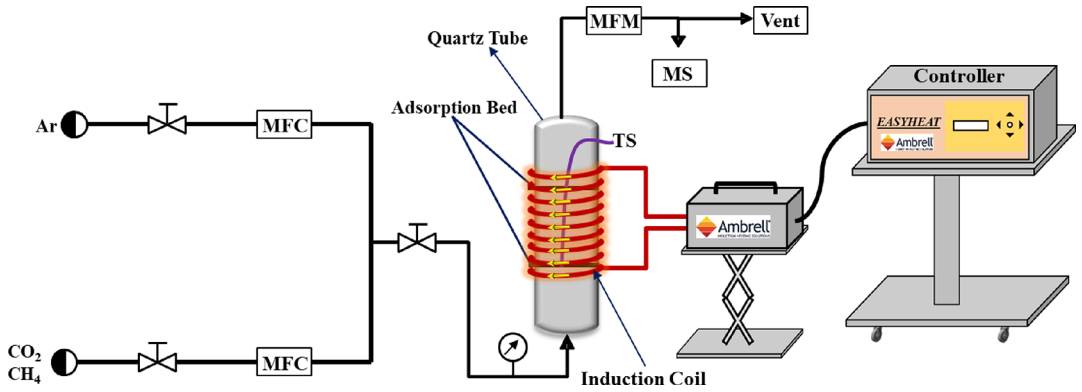

Figure 2. Schematic representation of the magnetic induction setup used in breakthrough experiments.

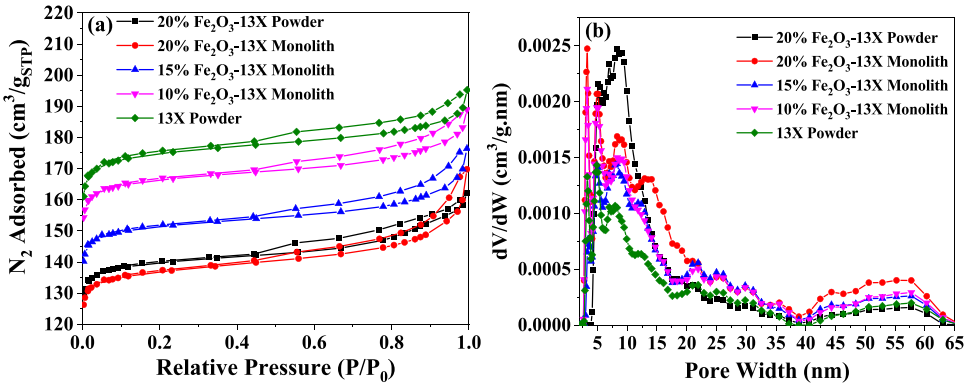

Figure 3. (a) N_2 physisorption isotherms at 77 K and (b) NLDFT PSD profiles for zeolite 13X and composite materials.

composite monoliths with 10, 15, and 20 wt % Fe_2O_3 loading in water and exposing them to the magnetic field, while recording the temperature gradients during magnetic induction. This test was repeated for the magnetic field strengths of 12.6, 21.4, and 31.4 mT to get the slope of the heating profile. The formula of the SAR calculation is shown in eq 1.

$$\mathrm{SAR} = C_S \frac{m_s}{m_m}\left(\frac{\mathrm{d}T}{\mathrm{d}t}\right)_{t=0} \quad (1)$$

where C_s, m_s, and m_m are, respectively, the specific heat capacity, weight of the suspension fluid (water), and the weight of magnetic particles.

2.4. Unary Adsorption Isotherm Measurements. The low-pressure CO_2 and CH_4 adsorption isotherms were collected on a Micromeritics 3Flex gas analyzer from 0 to 1 bar at 25, 35, and 55 °C. The samples were degassed at 350 °C for 6 h prior to the adsorption isotherm measurements. The CO_2/CH_4 selectivity values were calculated using the ideal adsorbed solution theory (IAST) method by fitting the unary isotherms with the Langmuir model and then estimating the IAST selectivities using the single component isotherms for a 50/50 binary gas composition.[24] Also, the enthalpies of adsorption (ΔH_{ads}) for CO_2 and CH_4 were estimated at capacities of 2.34 and 0.33 mmol/g, respectively, using the Clausius−Clapeyron method.[23]

2.5. Magnetic Induction Breakthrough Experiments. A glass bed with dimensions of 1.60 cm ID and length of 15.2 cm was used in the experiments. The materials were printed into monoliths of 200 cpsi with a length of ∼7.62 cm, and then loaded into the bed along with thermal wool and glass beads to fill the rest of the bed. It should be noted that the 200 cpsi monoliths were selected due to faster mass transfer kinetics and lower gas throttling.[25] The runs were carried out in-house using an Ambrell easy heat 0224 magnetic induction heating system. The amount of sorbent loaded in the bed was restricted to the coil size, which used 8 magnetic coils of 2″ diameter. The experiments consisted of the following four steps: (i) degassing, (ii) adsorption, (iii) desorption, and (iv) cooling. The gases were controlled by mass flow controllers (MFCs) from Brooks to allow for a constant flow rate of 40 mL/min and a Brooks mass flow meter (MFM) after the column with a mass spectrometer MKS to monitor the outlet flow rate and composition, respectively. Three magnetic induction intensities were used during the desorption step, namely, 12.6, 21.4, and 31.4 mT. The temperature response in real time was monitored using optic fiber TS-4 temperature sensors from Optocon. An overall layout of the system can be seen in Figure 2. For conventional heating runs, the coil was replaced with heating tape and a PID temperature controller.

3. RESULTS AND DISCUSSION

3.1. Material Characterization. The N_2 physisorption isotherms and the PSD profiles of the homogenously mixed 3D-printed magnetic monoliths and the control zeolite 13X powder are displayed in Figure 3a,b, and the corresponding textural properties are listed in Table 1. Like the bare zeolite, the composites displayed type I−IV isotherms, indicating a hierarchal microporous−mesoporous pore structure. The N_2 uptake over 5 μm Fe_2O_3 particles was negligible, and that is why their isotherms were not displayed. As evident from Figure 3a, the N_2 uptake over the composites decreased as the Fe_2O_3 loading increased in the 3D-printed monoliths.

https://doi.org/10.1021/acs.iecr.2c02969
Ind. Eng. Chem. Res. 2022, 61, 18843−18853

Table 1. Textural Properties of Bare Zeolite 13X and Fe_2O_3, and the Corresponding Composites

sample	S_{BET} (m^2/g)	V_{micro} (cm^3/g)	V_{meso} (cm^3/g)	d_p (nm)
13X monolith	553	0.25	0.045	3.3, 5, 9, 14, 21
30 nm Fe_2O_3 powder	21		0.053	3, 5
100 nm Fe_2O_3 powder	17		0.046	3, 5
5 μm Fe_2O_3 powder	12		0.027	3, 5
20% Fe_2O_3-13X powder	442	0.20	0.028	5, 7, 9
20% Fe_2O_3-13X monolith	435	0.19	0.046	3.3, 5, 9, 13, 21
15% Fe_2O_3-13X monolith	479	0.22	0.034	3.3, 5, 9, 13, 21
10% Fe_2O_3-13X monolith	526	0.23	0.032	3.3, 5, 9, 14, 21

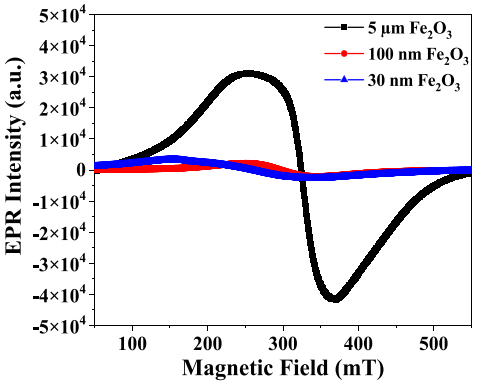

Figure 4. EPR spectra for 20% Fe_2O_3-13X powder with 5 μm, 100 nm, and 30 nm Fe_2O_3 particles.

Moreover, comparing the physisorption isotherms of 20% Fe_2O_3-13X powder and 20% Fe_2O_3-13X monolith, it was noted that the uptake at low partial pressures was slightly higher over the powder than over the monolith analogue, but it was reversed as the partial pressure (P/P_0) approached 1.0. This was expected as the presence of the binder and the plasticizer reduces the microporosity while enhancing the degree of the mesoporosity of the monolith. Notably, the shape of the H3 hysteresis loop remained consistent across the samples with the onset of the loop in each isotherm taking place at a P/P_0 of approximately 0.45.[26,27] The NLDFT PSD profiles in Figure 3b confirmed that the pore size distribution was not altered significantly in the composites relative to the bare zeolite, albeit the intensity of the peaks in each domain changed to some extent. The NLDFT method provides accurate estimation of pore size range based on the pore geometry of the material. This method tends to be more accurate for pores having sizes smaller than 10 nm.[28,29] For >10 nm pores, the Barrett, Joyner, and Halenda (BJH) method could be implemented to give a more accurate description of the mesoporosity of the adsorbent.[29]

From Table 1, the reduction in the surface area was found to be proportional to the percentage of Fe_2O_3 added to the paste, since the materials were physically mixed and the surface area of Fe_2O_3 was only ~13, 17, and 21 m^2/g for 5 μm, 100 nm, and 30 nm, respectively, while 13X exhibited a surface area of ~553 m^2/g. Similarly, the total pore volume was reduced by 4, 7, and 14% for the Fe_2O_3-13X monoliths with 10, 15, and 20 wt % Fe_2O_3 content, respectively, compared to the bare zeolite. Overall, these results highlighted that even though the textural properties of the composites were adversely affected by the addition of Fe_2O_3, the magnetic composites still possessed sufficient surface area and porosity for adsorptive separation of CO_2 and CH_4 in the biogas upgrading process.

The EPR tests were carried out to determine the degree of responsiveness of the magnetic composites with varying Fe_2O_3 particle sizes to the magnetic field. Magnetic wave absorptions as a function of magnetic field for 20% Fe_2O_3-13X physically mixed powders of 5 μm, 30 nm, and 100 nm particle sizes are presented in Figure 4. Generally speaking, larger particle size allows for an increased EPR spectrum absorbance. As clearly evident from this figure, the larger 5 μm Fe_2O_3 particles were more responsive to the magnetic field than the 30 and 100 nm particle sizes, indicated by the higher intensity in the 250−360 mT range compared to the 30 and 100 nm particle sizes. The importance of this response will be discussed more in section 3.3.1. On the basis of these EPR results, the composite monoliths were synthesized with only 5 μm-sized Fe_2O_3 and the remaining sections discuss the results for this set of magnetic monoliths.

3.2. Unary CO_2 and CH_4 Adsorption Isotherms. The unary adsorption isotherms of CO_2 and CH_4 obtained at 25 °C over the bare zeolite and the corresponding composites are shown in Figure 5. In agreement with the literature, the bare zeolite 13 X was more selective toward CO_2 than CH_4, with capacities comparable to the reported data. For both gases, the adsorption amounts decreased in the order of 13X > 10% Fe_2O_3-13X monolith >15% Fe_2O_3-13X monolith >20% Fe_2O_3-13X powder >20% Fe_2O_3-13X monolith. The reduction in CO_2 and CH_4 capacities of composites was proportional to the quantity of Fe_2O_3 added to the monolith mixture. It was also noted that the gas uptakes were almost exclusively related to the surface area (and porosity), confirming the physisorption of CO_2 and CH_4 on the pore surface. As also noted earlier, between the 20% Fe_2O_3-13X powder and monolith, a reduction in gas uptake (~15%) was observed for the monolith sample, which was almost proportional to the zeolite 13X content, indicating that the paste formulation and printing conditions did not deteriorate the adsorption properties of the sorbents, as reported in our previous works.[30,31]

The IAST CO_2/CH_4 selectivities estimated from the 25, 35, and 55 °C adsorption isotherms are reported in Table 2, along with the ΔH_{ads} values for CO_2 and CH_4. Similar selectivities were found across the composites with a ~6% fluctuation from the median, which further implied that the addition of Fe_2O_3 did not dramatically alter the properties of zeolite 13X in the magnetic composites. It should be noted that the selectivities were slightly higher than actual selectivity values reported in the literature; however, the IAST model usually overestimates the selectivity for binary gas mixtures, mainly because the model ignores the change in temperature during adsorption and interactions between adsorbate molecules, as pointed out by Bartholdy et al.[32] Moreover, the covariance between the parameters in the two-component Langmuir model can affect the robustness of the IAST analysis if they are left to be free-floating parameters for the regression analysis. Furthermore, the ΔH_{ads} values for CH_4 were lower than those for CO_2, as expected, which has been shown to range from −34 to −50 kJ/mol for zeolite 13X CO_2 adsorption.[33] Additionally, the estimated ΔH_{ads} values for the composites were found to be slightly lower than those for the bare sorbent (~12%), which could be due to the addition of the Fe_2O_3 and bentonite clay,

https://doi.org/10.1021/acs.iecr.2c02969
Ind. Eng. Chem. Res. 2022, 61, 18843−18853

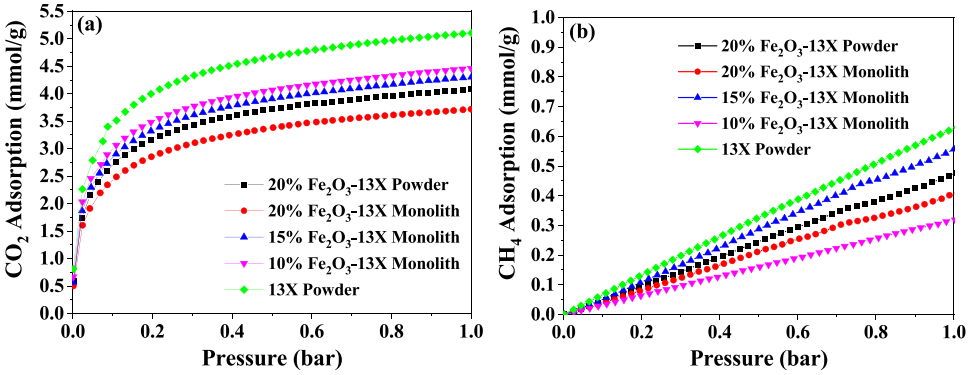

Figure 5. Unary adsorption isotherms of (a) CO_2 and (b) CH_4 over zeolite 13X and the corresponding composite materials.

Table 2. IAST Selectivity Values and Enthalpies of Adsorptions for Zeolite 13X and Composite Materials

sample	IAST selectivity (CO_2/CH_4)	$-\Delta H_{ads}$ CO_2 (kJ/mol)	$-\Delta H_{ads}$ CH_4 (kJ/mol)
13X monolith	7.5	47.9	21.5
20% Fe_2O_3-13X powder	8.3	34.7	15.5
20% Fe_2O_3-13X monolith	8.5	33.4	13.6
15% Fe_2O_3-13X monolith	8.2	35.7	17.4
10% Fe_2O_3-13X monolith	8.1	37.2	19.6

with a decreasing trend as Fe_2O_3 loading increased. Overall, these equilibrium adsorption isotherms and the corresponding calculations revealed the comparable performance of the magnetic composites to their parent zeolite 13X by demonstrating high CO_2 capture capacity and CO_2/CH_4 selectivity.

3.3. Dynamic Breakthrough Experiments. *3.3.1. Effect of Fe_2O_3 Particle Size.* As the EPR spectra demonstrated (Figure 4), particle size can have a dramatic impact on the effectiveness of the ferromagnetic materials; thus, we developed magnetic composites with varying particle size of Fe_2O_3 and assessed the degree of their responsiveness to the external magnetic field with a fixed intensity (ca. 31.4 mT). For induction heating, the energy expelled from the ferromagnetic material facilitates the regeneration; therefore, it is important to determine the heating capabilities of different particle sizes. Fe_2O_3 with 30 nm, 100 nm, and 5 μm particle sizes was mixed with zeolite 13X at the 20 wt % loading to determine the optimal particle size needed for magnetic induction. The temperature profiles in Figure 6 indicated that the larger particle size of 5 μm allowed for a faster heating, achieving a maximum temperature of 189 °C, compared to the 30 and 100 nm Fe_2O_3 particles, which reached only 65.2 and 64.9 °C maximum temperatures, respectively, when exposed to the same magnetic field intensity. This reduction in heating is due to the anisotropic energy that decreased as the particle size decreased, causing lower vibrations that heated the ferromagnetic material and therefore the sorbent.[34,35] The heating rate of the 5 μm sample was found to be larger than that of the 100 and 30 nm particle sizes by 60 and 65%, respectively. The cooling rates, on the other hand, were found to be similar for the three composites. On the basis of exhibiting a faster heating rate and achieving a higher desorption temperature, the 5 μm-size 20% Fe_2O_3-13X was concluded to outperform its composite analogues with smaller particle sizes, in agreement with the EPR test results (Table 3).

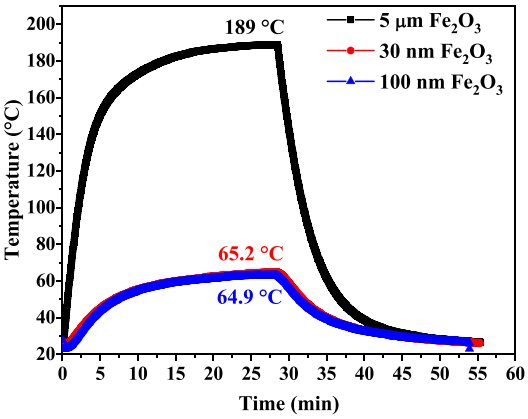

Figure 6. Temperature profiles for 20% Fe_2O_3-13X composite powders with Fe_2O_3 particle sizes of 5 μm, 30 nm, and 100 nm under a magnetic field strength of 31.4 mT.

Table 3. Thermal Characteristics of 20% Fe_2O_3-13X Powder Samples with Varying Particle Sizes under a Magnetic Field of 31.4 mT

sample	max. temperature (°C)	heating rate (°C/min)	cooling rate (min^{-1})
20% Fe_2O_3-13X powder (30 nm)	64.9	5.46	0.066
20% Fe_2O_3-13X powder (100 nm)	65.2	5.54	0.064
20% Fe_2O_3-13X powder (5 μm)	189.0	16.9	0.054

3.3.2. Magnetic Induction versus Conventional Heating. Monolithic structures usually give rise to a 60% lower pressure drop than the powder with a longer contact time with adsorbates due to the turbulent flow in the monolith.[30] To assess how structuring the sorbent powder into a monolithic contactor affects its desorption performance under induction heating, breakthrough tests were performed over 20% Fe_2O_3-13X powder and 20% Fe_2O_3-13X monolith samples (with 5 μm Fe_2O_3 particles), and the corresponding concentration and temperature profiles under both induction and conventional heating modes are depicted in Figure 7. Looking first at the concentration fronts in both cases (Figure 7a,c), an initial spike of CO_2 concentration release was the most striking feature of the induction heating, which essentially stemmed from the direct energy transfer from the magnetic field to the sorbent causing an instantaneous start to regeneration. It was also noted that due to the lower adsorption amount, the magnitude of the roll-over was smaller over the monolith than that over the powder sample. Moreover, under induction heating, the

https://doi.org/10.1021/acs.iecr.2c02969
Ind. Eng. Chem. Res. 2022, 61, 18843−18853

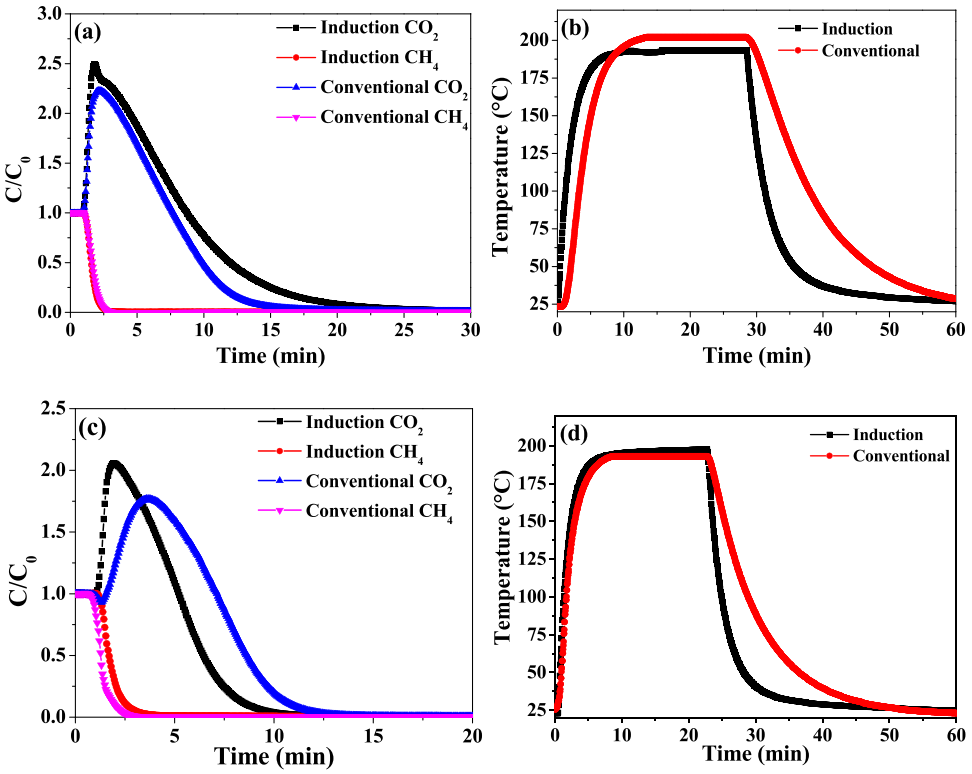

Figure 7. Concentration and temperature profiles for (a, b) 20% Fe_2O_3-13X powder and (c, d) 20% Fe_2O_3-13X monolith samples.

Table 4. Breakthrough Results of the Conventional and Induction Heating of the 5 μm-Size 20% Fe_2O_3-13X Powder and Monolith Samples

sample	heating mode	$q_{CO2,des}$(mmol/g)	$r_{CO2,95\%}$(mmol/g min)	heating rate (°C/min)	cooling rate (°C/min)
20% Fe_2O_3-13X powder	conventional	3.66	0.18	13.2	5.8
	induction	3.90	0.24	16.9	8.0
20% Fe_2O_3-13X monolith	conventional	2.71	0.15	10.9	5.5
	induction	2.81	0.25	14.2	5.9

powdered sorbent desorbed at a faster rate than the monolith, on the account of its higher Fe_2O_3 ammount due to the lack of binder needed. In Figure 7b,d, comparison of the temperature profiles indicated that under both heating modes, the bed temperature rises to almost the same temperature during desorption; however, it drops much quicker during cooling step in the case of induction relevant to the conventional case. Although the magnetic field has no direct influence on the cooling rate, the magnetic field targets only the sorbent, while the conventional heating must heat both the column wall and the sorbent. Therefore, the conventional heating process requires additional cooling due to the conduction of the column wall, thereby increasing the cooling step time.[12] However, it is important to emphasize the dilemma of the need for convective cooling to bring the temperature of the bed down to the adsorption temperature in the case of induction cooling. This can in fact serve as a drawback of this method since the cooling rate can very largely dictate the cycle time, similar to the conventional TSA process. It was also noted that compared with 20% Fe_2O_3-13X powder, the monolith analogue exhibited a faster heat transfer rate in both desorption and cooling steps, as expected. Monoliths usually display better thermal management due to the ability to thin walls, which can be accounted for by the external film resistance, which is channel-dependent, as demonstrated earlier.[36]

The quantification of the amount and rate of desorbed CO_2 ($q_{CO2,des}$ and $r_{CO2,95\%}$, respectively) along with heating and cooling rates is presented in Table 4. From these data, the induction heating resulted in a slightly faster desorption rate, which was 1.5 times greater than that in the case of conventional heating for the 20% Fe_2O_3-13X monolith. As also clear from this table, the cooling rates were found to be higher in the case of induction heating; for example, the 20% Fe_2O_3-13X monolith exhibited cooling rates of 5.5 and 5.9 °C/min under conventional and induction heating modes, respectively, which corresponded to 34 and 30 min cooling times. Overall, these findings highlight the efficacy of the induction heating in regenerating the composite sorbent at a rate comparable to (or even faster than) that under the conventional thermal desorption process. It is however necessary to optimize the material's properties for the induction heating process to create a reasonable balance between heating rate and adsorption capacity.

3.3.3. Effect of Monolith Composition. It is expected that the higher amount of ferromagnetic material in the composite enhances the heating rate during sorbent regeneration but at the expense of reduced adsorption capacity due to the smaller number of surface active sites. To develop efficient magnetic-responsive sorbents, it is therefore essential to address this trade-off and optimize the percentage of ferromagnetic

https://doi.org/10.1021/acs.iecr.2c02969
Ind. Eng. Chem. Res. 2022, 61, 18843−18853

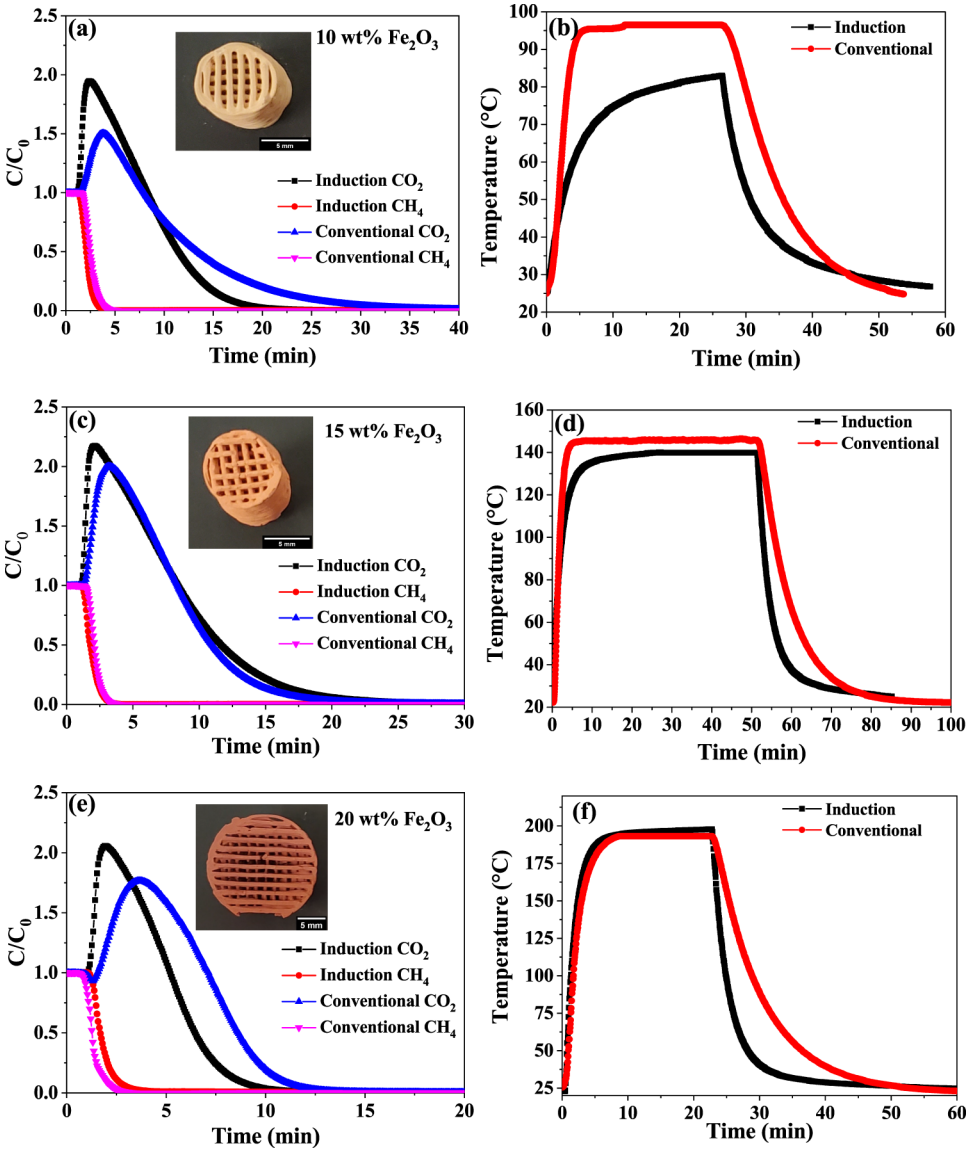

Figure 8. (a, c, e) Breakthrough desorption wavefronts and (b, d, f) temperature profiles for the composite monoliths with 10, 15, and 20 wt % Fe_2O_3 loading.

Table 5. Desorption, Heating, and Cooling Rates for the 10, 15, and 20% Fe_2O_3 Compositions Using Induction Heating

sample	heating mode	$q_{CO2,des}$(mmol/g)	$r_{CO2,des,95\%}$(mmol/g min)	heating rate (°C/min)	cooling rate (°C/min)	SAR (W/g)
10% Fe_2O_3-13X monolith	conventional	2.84	0.13	14.0	2.7	
	induction	3.35	0.17	3.2	2.7	9.28
15% Fe_2O_3-13X monolith	conventional	3.13	0.18	16.4	3.9	
	induction	3.17	0.19	5.7	4.7	9.98
20% Fe_2O_3-13X monolith	conventional	2.71	0.24	10.9	5.5	
	induction	2.81	0.25	14.2	5.4	10.63

material during magnetic composite synthesis. As shown in Figure 8, as the percent composition of ferromagnetic particles increased, the rate of heating and magnitude of temperature gradient increased. Under the same magnetic field (ca. 31.4 mT), the bed temperature rose to 80, 130, and 175 °C for Fe_2O_3-13X monoliths with 10, 15, and 20 wt % Fe_2O_3, respectively. This trend was found to be consistent with a previously reported study by Denayer and co-workers.[11] Initially, the heating from the induction was approximate to that of the conventional at a rate of 3.2, 5.7, and 14.2 °C/min for the 10, 15, and 20 wt % composites, respectively, but later, it took much longer for the materials to reach a maximum temperature under the induction heating. The lower heating rate in the 10 and 15 wt % monoliths can be attributed to lower loading of the Fe_2O_3 particles, which reduced sufficient contact with the zeolite 13X particles for efficient heat conduction, thereby causing the decrease in heating rate. Moreover, for all three samples, the CO_2 desorption rate under the induction heating was found to be much greater than that under the conventional heating at the same maximum

https://doi.org/10.1021/acs.iecr.2c02969
Ind. Eng. Chem. Res. 2022, 61, 18843−18853

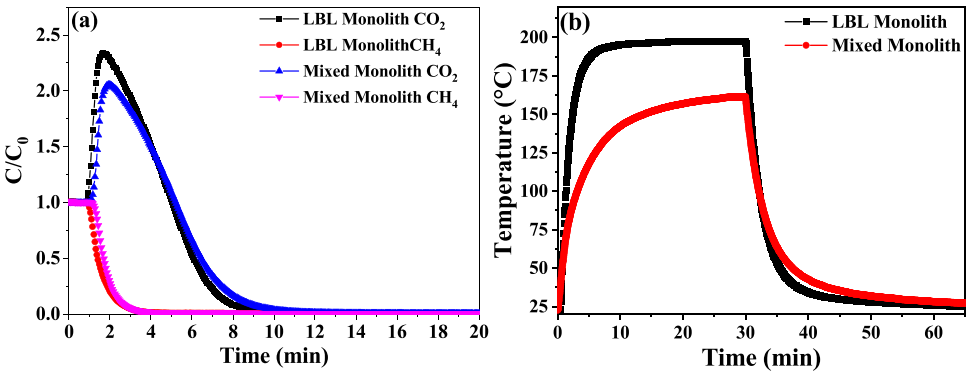

Figure 9. (a) Concentration fronts and (b) temperature profiles for the 20% Fe_2O_3-13X LBL and mixed monoliths at 31.4 mT and 1 bar.

Table 6. CO_2 Desorption Amount and Rate and Temperature Analysis of the 20% Fe_2O_3-13X Mixed and LBL Monoliths at 31.4 mT and 1 bar

samples	$q_{CO2,des}$(mmol/g)	$r_{CO2,des,95\%}$(mmol/g min)	heating rate (°C/min)	cooling rate (°C/min)
20% Fe_2O_3-13X mixed monolith	2.81	0.25	13.2	3.8
20% Fe_2O_3-13X LBL monolith	3.22	0.38	17.0	4.9

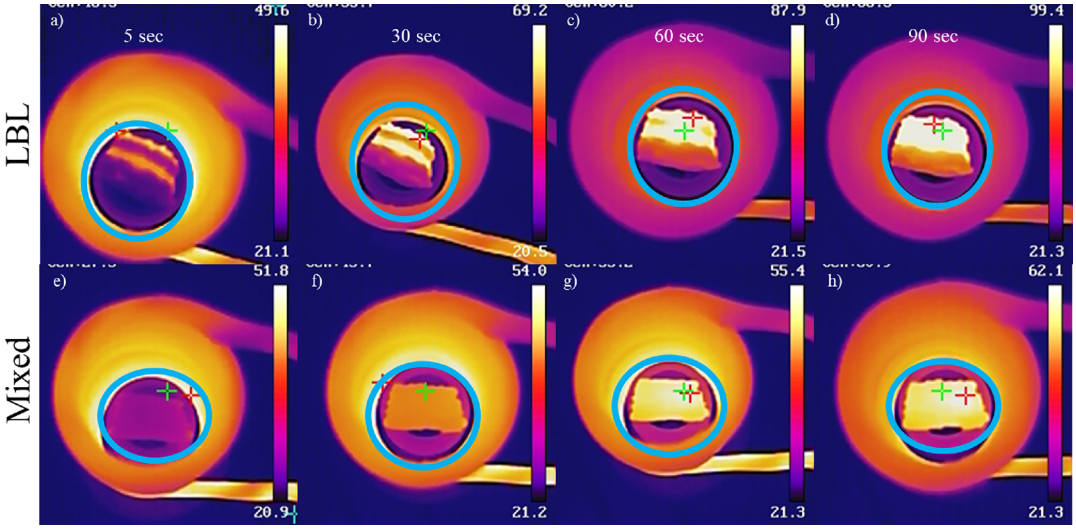

Figure 10. Thermal imaging time laps of 20% Fe_2O_3-13X (a–d) LBL and (e–h) mixed monoliths at time intervals of (a, e) 5, (b, f) 30, (c, g) 60, and (d, h) 90 s. All monoliths are indicated by the blue circle.

temperatures, with a spike at the initial start of the desorption due to the direct energy transfer to the monolith.

Table 5 tabulates the rate and amount of CO_2 desorption during induction and conventional heating modes along with heating and cooling rates for the three composite monoliths studied here. As evident, the amount desorbed was lower for the 20 wt % composite but at a faster rate compared with the other two samples, which may be due to lower uptake of gas during adsorption step. Similarly for this sample, heating and cooling rates were estimated to be 14.2 and 5.4 (°C/min), respectively, which were approximately 4.4 and 2.0 times faster than those for the 10 wt % analogue. The faster cooling rate for this sample can be attributed to the larger difference between the room temperature and the bed; nevertheless, the cooling steps for 10% and 15% Fe_2O_3-13X monoliths were shorter due to the lower temperatures. For example, the 20% Fe_2O_3-13X monolith was completely desorbed at approximately 8.6 min, and the temperature of the monolith at that point was approximately 138.6 °C, as compared to the conventional heating, which was already up to the target temperature. Moreover, the SAR values of the 10, 15, and, 20 wt % Fe_2O_3-13X monoliths at 32.4 mT estimated to be 9.28, 9.98, and 10.63 W/g, which further verified that the increased Fe_2O_3 content actually helps increase the efficiency of the induction heating.

3.3.4. Effect of Monolith Configuration. In the next step, to demonstrate how the monolith configuration affects the desorption and heating rate under induction heating, we performed adsorption–desorption tests using 3D-printed 20% Fe_2O_3-13X monoliths prepared via homogenously mixed and LBL extrusion methods. Under identical conditions, the mixed monoliths achieved a maximum temperature of 150 °C, whereas the LBL monolith heated to 185 °C, as shown in Figure 9a. This caused more CO_2 molecules to desorb from the sorbent (3.22 vs 2.81 mmol/g, see Table 6). At the same time, the desorption rate of CO_2 from the LBL monolith was approximately 33% faster than that from the mixed monolith (0.38 vs 0.25 °C/min), as indicated by the larger initial peak

https://doi.org/10.1021/acs.iecr.2c02969
Ind. Eng. Chem. Res. 2022, 61, 18843–18853

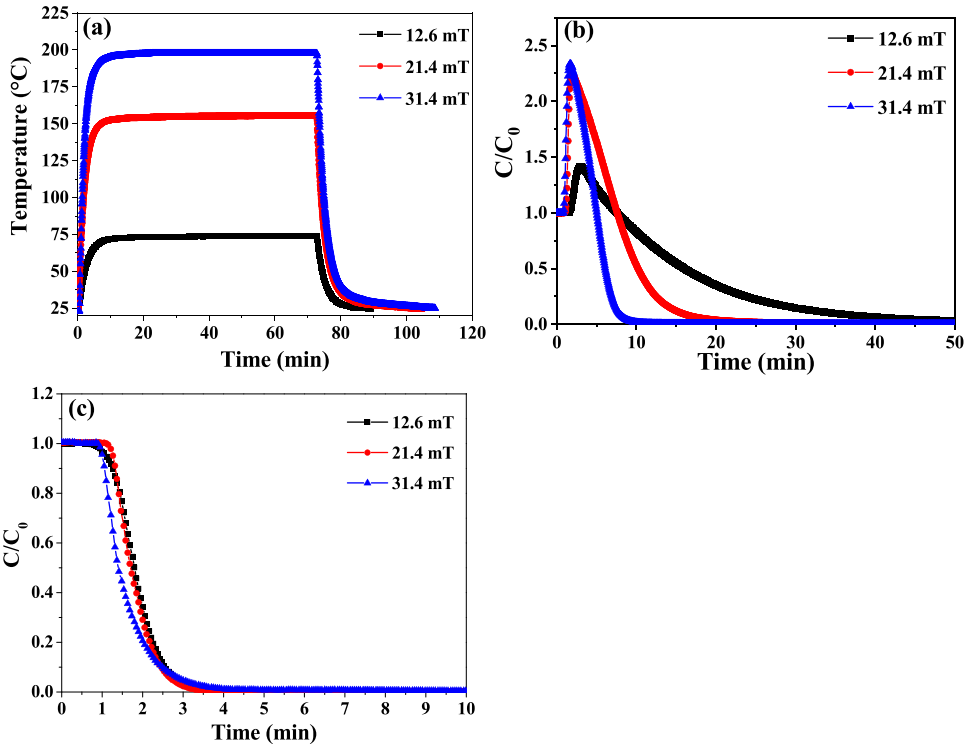

Figure 11. (a) Comparison of temperature profiles and desorption profiles for (b) CO_2 and (c) CH_4 over the 20% Fe_2O_3-13X LBL monolith under magnetic fields of 12.6, 21.4, and 31.4 mT.

and shorter desorption time (Figure 9b), which was believed to be caused by the larger maximum temperature in this bed. It is important to point out here that since the densities of the two monoliths with the same composition were different (2.2 and 2.6 g/cm^3 for homogenously mixed and LBL monoliths, respectively), it is expected that the volumetric capacity of the mixed monolith is higher than that of the LBL monolith. This is due to the higher amount of binder necessary to print the LBL monoliths. As with cooling, the LBL monolith outperformed its mixed monolith counterpart by displaying 4.9 (°C/min) cooling rate as opposed to 3.8 (°C/min) for the mixed sample. It is argued that in the LBL monolith, due to higher localized concentration of Fe_2O_3 particles, the magnitude of localized heat generated is higher, thereby allowing for a faster heat transfer to the 13X layers, as seen in Figure 10, while at the same time, the transport of the generated heat can be facilitated by the enhanced magnetic particles vibrations, as opposed to the mixed monolith where the Fe_2O_3 particles are separated from one another and localized concentration of these particles is far less than that in the LBL monolith. Nevertheless, it is worth mentioning that the LBL printing strategy may lead to heat sinks within the monolith when exposed to strong magnetic fields. Although more work needs to be done to assess the impact of the contactor's structure on adsorptive performance of the magnetic sorbents, these results highlight the importance of not only optimizing the composition but also the design of magnetic sorbent structures to enhance their magnetic responsiveness and thereby their separation performance.

3.3.5. Effect of Magnetic Field Strength. The induction intensity controls the energy delivered to the sorbent from the external magnetic field. Thus, it is important to determine if there is a more efficient magnetic field intensity or if the higher-powered field is always better. This experiment used 100, 170, and 250 A, which converts to 12.6, 21.4, and 31.4 mT. Under these three magnetic fields, the 20% Fe_2O_3-13X LBL monolith was tested and the corresponding CO_2 and CH_4 concentration profiles during desorption along with the temperature profiles were recorded, as illustrated in Figure 11. Comparison of the temperature profiles in Figure 11a revealed that the 12.6 mT field intensity is not sufficient to attain a high temperature gradient needed to fully regenerate the sorbent, but as the magnetic field strength increased to 21.4 and 31.4 mT, higher temperature gradients were observed (120 and 170 °C, respectively).

As evident from Figure 11b, the 31.4 mT magnetic field gave rise to a faster CO_2 desorption rate than that of the 12.6 and 21.4 mT fields by 80% and 53%, respectively, as also evident from the data listed in Table 7. This indicated that a stronger magnetic field (>31 mT) is required to achieve higher efficiency in terms of desorption rate with scaling energy intensity. However, the CH_4 desorption rate was not changed drastically (Figure 11c), which could be due to the lower amount of this gas adsorbed on the sorbent during the adsorption step. The overall cycle time was reduced with the 31.4 mT as well since the desorption time was greatly reduced, and the cooling time was only marginally increased for the 12.6

Table 7. Desorption Rates and Temperature Analysis of the 20% Fe_2O_3-13X LBL Monolith under Magnetic Field Intensities of 12.6, 21.4, and 31.4 mT at 1 bar

induction intensity (mT)	$r_{CO2,des,95\%}$ (mmol/g min)	$r_{CH4,des,95\%}$ (mmol/g min)	heating rate (°C/min)	cooling rate (°C/min)
12.6	0.07	0.09	4.7	7.5
21.4	0.18	0.11	12.8	10.8
31.4	0.38	0.13	17.0	11.2

https://doi.org/10.1021/acs.iecr.2c02969
Ind. Eng. Chem. Res. 2022, 61, 18843−18853

and 21.4 mT runs. This further indicated that the higher magnetic field intensity is more effective due to the stronger coupling of locally induced eddy currents within the material.[37] These findings demonstrated that higher induction intensity drastically shortens the desorption time and correlates to a higher desorption temperature; however, since the distance from the coil to the column does have an important role in the induction heating, more testing will need to be conducted at larger beds to better characterize the impact of the field intensity on the sorbent regeneration and desorption rates.

4. CONCLUSIONS

This study formulated magnetic composite monoliths comprising ferromagnetic Fe_2O_3 and zeolite 13X to demonstrate the effectiveness of the magnetic induction heating in the biogas upgrading process. Specifically, the advantages of induction heating over conventional heating for the separation of CO_2/CH_4 over magnetic monoliths were demonstrated via dynamic breakthrough experiments. The results indicated that a large particle size is necessary for Fe_2O_3 to enhance the heating efficiency of the structured composites and to stay competitive to the conventional thermal heating method. Magnetic particle size and field intensity were found to inversely affect the temperature profiles during desorption. More magnetic characterization is necessary to better understand the magnetic response of Fe_2O_3-13X composites and further optimize their regenration during desorption. The vibration mechanism will also need to be studied to further confirm that 5 μm Fe_2O_3 gives off more energy than the 100 and 30 nm particles. It was also found that monolithic designs have a similar initial heating rate but cannot heat to a maximum temperature as efficiently as conventional heating systems. However, the composite sorbents regenerated before they reached their maximum temperature, indicating that the energy is being transferred to initiate adsorbate desorption directly from the ferromagnetic particles. This reduction allows for faster cycle times by enhancing the regeneration and reducing the cooling cycle since the material is fully regenerated at a lower temperature than in the case of conventional heating. Moreover, in the LBL monoliths, the pure sections of Fe_2O_3 allowed the whole monolith to heat up faster than if it was premixed into the monolith, indicating that this printing strategy offers a better approach in achieving faster heating and cooling rates compared to the homogenously mixed approach. Overall, this study indicates the potential for induction heating as an alternative process to conventional heating for biogas upgrading processes.

AUTHOR INFORMATION

Corresponding Author

Fateme Rezaei − *Linda and Bipin Doshi Department of Chemical and Biochemical Engineering, Missouri University of Science and Technology, Rolla, Missouri 65409-1230, United States;* orcid.org/0000-0002-4214-4235; Email: rezaeif@mst.edu

Authors

Kyle Newport − *Linda and Bipin Doshi Department of Chemical and Biochemical Engineering, Missouri University of Science and Technology, Rolla, Missouri 65409-1230, United States*

Khaled Baamran − *Linda and Bipin Doshi Department of Chemical and Biochemical Engineering, Missouri University of Science and Technology, Rolla, Missouri 65409-1230, United States*

Ali A. Rownaghi − *Department of Chemistry, Cleveland State University, Cleveland, Ohio 44115, United States;* orcid.org/0000-0001-5228-5624

Complete contact information is available at: https://pubs.acs.org/10.1021/acs.iecr.2c02969

Notes

The authors declare no competing financial interest.

ACKNOWLEDGMENTS

The authors thank the National Science Foundation (NSF IIP 2044726) for financially supporting this project.

REFERENCES

(1) *Energy Roadmap 2050*, Luxembourg: Publications Office of the European Union, 2012, 1−24.

(2) Speight, J.*Natural Gas: A Basic Handbook*; Gulf Professional Publishing, 2018.

(3) Bacsik, Z.; Cheung, O.; Vasiliev, P.; Hedin, N. Selective Separation of CO_2 and CH_4 for Biogas Upgrading on Zeolite NaKA and SAPO-56. *Appl Energy* **2016**, *162*, 613−621.

(4) Francl, J.; Kingery, W. D. Experimental Investigation of Effect of Porosity on Thermal Conductivity. *Thermal Conductivity IX* **1954**, *37*, 99−107.

(5) Sholl, D. S.; Lively, R. P. Seven Chemical Separations to Change the World. *Nature* **2016**, *532*, 6−437.

(6) Creutzig, F. Fuel Crisis: Slash Demand in Three Sectors. *Nature* **2022**, *606*, 460.

(7) Weiland, P. Biogas Production: Current State and Perspectives. *Appl. Microbiol. Biotechnol.* **2010**, *85*, 849−860.

(8) Scholz, M.; Frank, B.; Stockmeier, F.; Falß, S.; Wessling, M. Techno-Economic Analysis of Hybrid Processes for Biogas Upgrading. *Ind. Eng. Chem. Res.* **2013**, *52*, 16929−16938.

(9) Verougstraete, B.; Schoukens, M.; Sutens, B.; Haute, H.; Yoran, V.; Rombouts, M.; Denayer, J. Electrical Swing Adsorption on 3D-Printed Activated Carbon Monoliths for CO_2 Capture from Biogas. *Sep. Purif. Technol.* **2022**, *299*, No. 121660.

(10) Bauer, F.; Persson, T.; Hulteberg, C.; Tamm, D. Biogas Upgrading - Technology Overview, Comparison and Perspectives for the Future. *Biofuels, Bioprod. Biorefin.* **2013**, *7*, 499−511.

(11) Gholami, M.; Verougstraete, B.; Vanoudenhoven, R.; Baron, G. V.; van Assche, T.; Denayer, J. F. M. Induction Heating as an Alternative Electrified Heating Method for Carbon Capture Process. *Chem. Eng. J.* **2022**, *431*, No. 133380.

(12) Baamran, K.; Newport, K.; Rownaghi, A. A.; Rezaei, F. Development and Assessment of Magnetic Fe_2O_3@MOF-74 Composite. *Chem. Eng. J.* **2023**, *451*, No. 139006.

(13) Gomez-Rueda; Verougstraete, B.; Ranga, C.; Perez-Botella, E.; Reniers, F.; Denayer, J. Rapid Temperature Swing Adsorption Using Microwave Regeneration for Carbon Capture. *Chem. Eng. J.* **2022**, 446.

(14) Wang, M.; Zhou, S.; Cao, S.; Wang, Z.; Liu, S.; Wei, S.; Chen, Y.; Lu, X. Stimulus-Responsive Adsorbent Materials for CO_2 capture and Separation. *J. Mater. Chem. A* **2020**, *8*, 10519−10533.

(15) Lin, X.; Shao, B.; Zhu, J.; Pan, F.; Hu, J.; Wang, M.; Liu, H. In Situ Electromagnetic Induction Heating for CO_2 Temperature Swing Adsorption on Magnetic Fe_3O_4/N-Doped Porous Carbon. *Energy Fuels* **2020**, *34*, 14439−14446.

(16) Sadiq, M. M.; Rubio-Martinez, M.; Zadehahmadi, F.; Suzuki, K.; Hill, M. R. Magnetic Framework Composites for Low Concentration Methane Capture. *Ind. Eng. Chem. Res.* **2018**, *57*, 6040−6047.

(17) Li, H.; Hill, M. R. Low-Energy CO_2 Release from Metal-Organic Frameworks Triggered by External Stimuli. *Acc. Chem. Res.* **2017**, *50*, 778−786.

(18) Sadiq, M. M.; Li, H.; Hill, A. J.; Falcaro, P.; Hill, M. R.; Suzuki, K. Magnetic Induction Swing Adsorption: An Energy Efficient Route to Porous Adsorbent Regeneration. *Chem. Mater.* **2016**, *28*, 6219−6226.
(19) Melag, L.; Sadiq, M. M.; Konstas, K.; Zadehahmadi, F.; Suzuki, K.; Hill, M. R. Performance Evaluation of CuBTC Composites for Room Temperature Oxygen Storage. *RSC Adv.* **2020**, *10*, 40960−40968.
(20) Chan, K. C.; Chao, C. Y. H.; Wu, C. L. Measurement of Properties and Performance Prediction of the New MWCNT-Embedded Zeolite 13X/$CaCl_2$ Composite Adsorbents. *Int. J. Heat Mass Transfer* **2015**, *89*, 308−319.
(21) Aittomäki, A.; Aula, A. Determination of Effective Thermal Conductivity of Adsorbent Bed Using Measured Temperature Profiles. *Int. Commun. Heat Mass Transfer* **1991**, *18*, 681−690.
(22) Wang, L. W.Thermal Conductivity and Permeability of Consolidated Expanded Natural Graphite Treated with Suphuric Acid. *Sci. Direct* , *49* (), 4812−4819, DOI: 10.1016/j.carbon.2011.06.093.
(23) Giraldo, L.; Rodriguez-Estupiñán, P.; Moreno-Piraján, J. C. Isosteric Heat: Comparative Study between Clausius-Clapeyron, CSK and Adsorption Calorimetry Methods. *Processes* **2019**, *7*, 203.
(24) Chen, J.; Loo, L. S.; Wang, K. An Ideal Absorbed Solution Theory (IAST) Study of Adsorption Equilibria of Binary Mixtures of Methane and Ethane on a Templated Carbon. *J. Chem. Eng. Data* **2011**, *56*, 1209−1212.
(25) Lawson, S.; Adebayo, B.; Robinson, C.; Al-Naddaf, Q.; Rownaghi, A. A.; Rezaei, F. The Effects of Cell Density and Intrinsic Porosity on Structural Properties and Adsorption Kinetics in 3D-Printed Zeolite Monoliths. *Chem. Eng. Sci.* **2020**, *218*, No. 115564.
(26) Chen, C.; Park, D. W.; Ahn, W. S. CO_2 Capture Using Zeolite 13X Prepared from Bentonite. *Appl. Surf. Sci.* **2014**, *292*, 63−67.
(27) Thommes, M.; Kaneko, K.; Neimark, A. V.; Olivier, J. P.; Rodriguez-Reinoso, F.; Rouquerol, J.; Sing, K. S. W. Physisorption of Gases, with Special Reference to the Evaluation of Surface Area and Pore Size Distribution (IUPAC Technical Report). *Pure Appl. Chem.* **2015**, *87*, 1051−1069.
(28) Bernet, T.; Pinerio, M.; Plantier, F.; Miqueu, C. A 3D Non-Local Density Functional Theory for Any Pore Geometry. *Mol. Phys.* **2020**, *118*, 9−10.
(29) Villarroel-Rocha, J.; Barrera, D.; Sapag, K. Introducing a Self-Consistent Test and the Corresponding Modification in the Barrett, Joyner and Halenda Method for Pore-Size Determination. *Microporous Mesoporous Mater.* **2014**, *200*, 68−78.
(30) Lawson, S.; Li, X.; Thakkar, H.; Rownaghi, A. A.; Rezaei, F. Recent Advances in 3D Printing of Structured Materials for Adsorption and Catalysis Applications. *Chem. Rev.* **2021**, *121*, 6246−6291.
(31) Thakkar, H.; Eastman, S.; Hajari, A.; Rownaghi, A.; Knox, J.; Rezaei, F. 3D-Printed Zeolite Monoliths for CO_2 Removal from Enclosed Environments. *Appl. Mater. Interfaces* **2016**, *8*, 27753.
(32) Bartholdy, S.; Bjorner, M.; Solbraa, E.; Shapiro, A.; Kontogeorgis, G. Capabilities and Limitations of Predictive Engineering Theories for Multicomponent Adsorption. *Ind. Eng. Chem. Res.* **2013**, *52*, 11552−11563.
(33) Tom, R.; Sunil, P.; Stijn, P.; Pieterjan, V.; Dirk, V.; Gino, B.; Joeri, D. Selective Dynamic CO_2 Separations on Mg-MOF-74 at Low Pressures: A Detailed Comparison with 13X. *J. Phys. Chem. C* **2013**, *117*, 9301−9310.
(34) Abdellahi, M.; Tajally, M.; Mirzaee, O. The Effect of the Particle Size on the Heating and Drug Release Potential Of. *J. Magn. Magn. Mater.* **2021**, *530*, No. 167938.
(35) Spaldin, N. A.*Magnetic Materials: Fundamentals and Applications*, 2nd ed.; Cambridge University Press, 2010, DOI: 10.1017/CBO9780511781599.
(36) Rezaei, F.; Webley, P. Structured Adsorbents in Gas Separation Processes. *Sep. Purif. Technol.* **2010**, *12*, 243−256.
(37) Ahn, D.; Hong, S. A Study on Magnetic Field Repeater in Wireless Power Transfer. *IEEE Trans. Ind. Electron.* **2013**, *60*, 360−371.

https://doi.org/10.1021/acs.iecr.2c02969
Ind. Eng. Chem. Res. 2022, 61, 18843−18853